Deep Learning for Size-Agnostic Inverse Design of Random-Network 3D Printed Mechanical Metamaterials

Pahlavani, Helda; Tsifoutis-Kazolis, Kostas; Saldivar, Mauricio C.; Mody, Prerak; Zhou, Jie; Mirzaali, Mohammad J.; Zadpoor, Amir A.

DOI
10.1002/adma.202303481

Publication date
2023

Document Version
Final published version

Published in
Advanced Materials

Citation (APA)
Pahlavani, H., Tsifoutis-Kazolis, K., Saldivar, M. C., Mody, P., Zhou, J., Mirzaali, M. J., & Zadpoor, A. A. (2023). Deep Learning for Size-Agnostic Inverse Design of Random-Network 3D Printed Mechanical Metamaterials. *Advanced Materials*, *36 (2024)*(6), Article 2303481. https://doi.org/10.1002/adma.202303481

ADVANCED MATERIALS
www.advmat.de

Deep Learning for Size-Agnostic Inverse Design of Random-Network 3D Printed Mechanical Metamaterials

Helda Pahlavani, Kostas Tsifoutis-Kazolis, Mauricio C. Saldivar, Prerak Mody, Jie Zhou, Mohammad J. Mirzaali,* and Amir A. Zadpoor*

Practical applications of mechanical metamaterials often involve solving inverse problems aimed at finding microarchitectures that give rise to certain properties. The limited resolution of additive manufacturing techniques often requires solving such inverse problems for specific specimen sizes. Moreover, the candidate microarchitectures should be resistant to fatigue and fracture. Such a multi-objective inverse design problem is formidably difficult to solve but its solution is the key to real-world applications of mechanical metamaterials. Here, a modular approach titled "Deep-DRAM" that combines four decoupled models is proposed, including two deep learning (DL) models, a deep generative model based on conditional variational autoencoders, and direct finite element (FE) simulations. Deep-DRAM integrates these models into a framework capable of finding many solutions to the posed multi-objective inverse design problem based on random-network unit cells. Using an extensive set of simulations as well as experiments performed on 3D printed specimens, it is demonstrate that: 1) the predictions of the DL models are in agreement with FE simulations and experimental observations, 2) an enlarged envelope of achievable elastic properties (e.g., rare combinations of double auxeticity and high stiffness) is realized using the proposed approach, and 3) Deep-DRAM can provide many solutions to the considered multi-objective inverse design problem.

1. Introduction

The second and third decades of the 21st century have witnessed the emergence of architected materials with bespoke, unusual properties that stem from their small-scale design. At the nexus of rational design techniques, where computational models are used to establish design–property relationships, and additive manufacturing (AM), i.e., 3D printing, techniques, which enable the realization of arbitrarily complex designs, a highly vibrant subdiscipline has emerged that is rapidly pushing such designer materials into applications in medical devices,[1–3] soft robotics,[4–6] and other advanced areas of research.[7–9] Depending on the type of the properties targeted, these architected materials may be referred to as mechanical metamaterials,[10–14] acoustic metamaterials,[15–17] or meta-biomaterials,[3,18] among other types.

Despite their recent academic success, there are two major challenges that hinder the real-world applications of metamaterials in general and mechanical metamaterials in particular. To put these challenges in perspective, let us consider a typical device design scenario where the required elastic properties as well as the dimensions of a device are specified by the device designer. The design problem is then reduced to the problem of finding the microarchitectures that give rise to the required elastic properties, while also satisfying the size requirements. The inverse problem of finding the microarchitecture(s) resulting in a specific set of elastic properties is challenging enough in its own right particularly given that the desired combination of properties is often very rare (e.g., high stiffness and highly negative values of the Poisson's ratio[19]). The difficulty of such an inverse design problem is further exacerbated by the fact that most mechanical metamaterials are usually only analyzed in terms of their homogenized or asymptotic properties (i.e., when the number of the constituting unit cells approaches infinity). Such homogenized solutions are only valid at their convergence limits and may significantly deviate from the actual elastic properties when the number of unit cells is not large enough[20] Given the limited resolution of AM techniques, it is often impossible to fit a very large number of unit cells within a given set of dimensions. Homogenized solutions may, therefore, not offer too much help

H. Pahlavani, K. Tsifoutis-Kazolis, M. C. Saldivar, J. Zhou, M. J. Mirzaali, A. A. Zadpoor
Department of Biomechanical Engineering
Faculty of Mechanical
Maritime and Materials Engineering
Delft University of Technology (TU Delft)
Mekelweg 2, Delft 2628 CD, The Netherlands
E-mail: h.pahlavani@tudelft.nl; m.j.mirzaali@tudelft.nl

P. Mody
Division of Image Processing (LKEB)
Radiology
Leiden University Medical Center (LUMC)
Albinusdreef 2, Leiden 2333 ZA, The Netherlands

The ORCID identification number(s) for the author(s) of this article can be found under https://doi.org/10.1002/adma.202303481

DOI: 10.1002/adma.202303481

when dealing with real-world design problems. The inverse design problem should, therefore, not be solved for the asymptotic case of an infinite number of unit cells but for the actual case of a finite number of unit cells in each spatial direction. Here, we use deep learning (DL) models and deep generative models to tackle such a size-agnostic inverse design problem within the context of random-network (RN) mechanical metamaterials.

Most of the mechanical metamaterials developed to date are composed of periodic unit cells. Previous studies have, however, shown that RN units cells, consisting of stretch- and bending-dominated beam-like structures, allow for a wide range of conventional and auxetic elastic properties,[21–25] which may go beyond the limits achieved by geometrically-ordered mechanical metamaterials, particularly when seeking after rare combinations of elastic properties[21] We will, therefore, use RN designs to increase the chance of finding accurate solutions for the inverse design problems targeted here. A facet of such nonlinear inverse problems relevant to microarchitecture design of mechanical metamaterials concerns the nonuniqueness of the solution. It is important to realize that different solutions to the inverse problem posed in the previous paragraph are not equal in many other aspects. That is because designs with similar effective properties could have highly different stress distributions and, thus, highly different degrees of resistance to fatigue and fracture. We are, therefore, interested to find as many of solutions to the posed inverse problem as possible so that additional design requirements, such a uniform stress distribution or a minimum stress peak, can be applied. This further increases the practical utility of the approach presented here.

The existing DL models used for such inverse-design problems are often deterministic in nature. Such models are not well equipped to regress a single input to multiple outputs and may converge to the average of the solutions instead. We will, therefore, model the aforementioned inverse design problem in a probabilistic, generative manner because such approaches have been shown to enable investigations of the structure–response relationship and can resolve the one-to-many mapping problem that deterministic models are unable to cope with.[26–29] Generative adversarial networks (GAN)[30] and variational autoencoders (VAE)[31] which seek to understand the underlying relationship between design features and targets/labels and generate new designs from a low-dimensional latent space, are popular deep generative models used for the inverse design of materials[27,32–35] and their multiscale microarchitectures.[36,37] In contrast to VAE, which provides a straightforward mapping from the observed dataset to a continuous latent space, a continuous latent space with a meaningful structure is intractable for GAN models[27] particularly in 3D.[38]

To achieve the goals presented above, we take a modular approach, hereafter referred to as "Deep-DRAM." Deep-DRAM (DL for the design of RN metamaterials) is composed of a sequence of DL and generative models that not only collectively solve the size-agnostic, inverse design problem but can also be (individually) used for many other purposes. First, we create a DL-based forward predictor model that predicts the anisotropic elastic properties of a specific type of RN unit cells. Second, we present a generative model based on conditional variational autoencoder (CVAE) that generates the microarchitecture of RN unit cells with a given set of anisotropic elastic properties. The third module is a DL-based forward predictor model that receives the microarchitecture of the RN unit cells and the desired dimensions of the specimen (i.e., the number of RN unit cells along each spatial direction) and predicts its elastic properties. The developed models are then combined to solve the size-agnostic design problem with the additional requirement that the maximum stresses are minimized (see Movies S1, S2, and S3, Supporting Information). While the data required for training and testing the DL models are all generated using finite element (FE) models, we also present several experiments in which actual mechanical metamaterials are 3D printed and mechanically tested to compare their measured elastic properties and deformation patterns with our computational results.

2. Results

2.1. Elastic Properties of RN Unit Cells

For the first module, we considered RN unit cells composed of 16 nodes ($n_x \times n_y$, $n_x = n_y = 4$) because this number of nodes allows for a broader range of elastic properties when compared to larger sizes of RN unit cells (Figure S2 and Table S1, Supporting Information), as well as a higher chance of extreme negative and extreme positive Poisson's ratios (Table S2, Supporting Information). For this number of nodes, it is possible to generate unit cells with average nodal connectivity values of $Z_g = 2.5$, 3, 3.5, 4, and 4.5. Depending on the Z_g value, the number of beam-like elements in the RN unit cells varied between 20 and 42 (**Figure 1**a). It should be noted that the total estimated number of unit cells that can be generated, whether they abide by the design limitations or not, considering the above-mentioned values of Z_g is $\approx 9.22 \times 10^{11}$ (Table S3, Supporting Information). Assuming that the average simulation time per design equals $\approx 5.42 \times 10^{-4}$ s (Figure S3, Supporting Information), it takes ≈497 million seconds (= 5761 days) (Table S3, Supporting Information) to perform FE analysis on all these RN unit cells. The huge number of possible designs highlights the need to have an ultrafast model to predict the elastic properties of the RN unit cells.

We performed FE analysis on 6 million randomly generated RN unit cells (i.e., 1.2 million unit cells from each group of Z_g) as the training group. The elastic properties in directions 1 and 2, which were calculated by FE modeling of these unit cells, cover a cone-like region with a range of (0, 0.25) and (−1.5, 1.2) for the relative elastic moduli (E_{11}/E_b and E_{22}/E_b, where E_b is the elastic modulus of the bulk material) and Poisson's ratios (ν_{12} and ν_{21}), respectively (Figure 1b). The distributions of the relative elastic modulus and Poisson's ratio in directions 1 and 2 had similar ranges of values. Moreover, the results show that the RN unit cells are highly anisotropic. The broad range of the elastic properties is due to the possibility to generate both stretching- and bending-dominated structures using random distributions of elements as well as by changing Z_g. These results confirm that it is possible to devise RN unit cells with extreme positive and extreme negative values of the Poisson's ratio as well as rare-event[19] double-auxetic unit cells.

We selected six unit cells from the different groups of elastic properties, i.e., almost extreme positive and negative values of the Poisson's ratio in one direction, almost extreme double-auxeticity, almost extreme elastic moduli in both directions, and

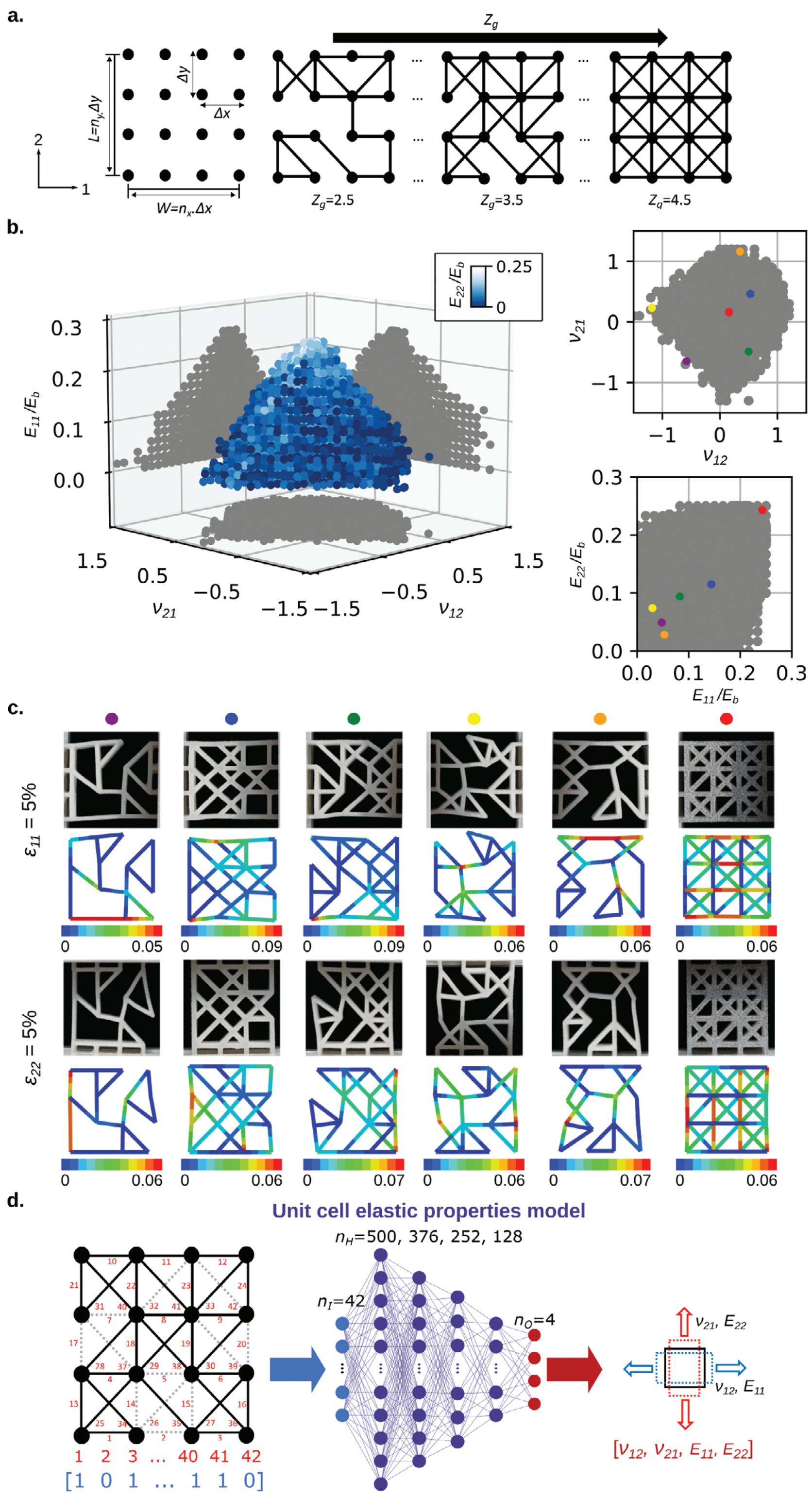

Figure 1. A schematic illustration and elastic properties of the RN unit cells as well as the network architecture of the unit cell elastic properties model. a) To design the RN unit cells, we predefined the node coordinates with a fixed horizontal and vertical distance of $\Delta x = \Delta y = 7.5$ mm. Assuming a grid of 4 × 4 nodes, the overall dimensions of each unit cell is $L = W = 22.5$ mm. Based on the defined overall connectivity, Z_g, the applicable number of beam-like elements were randomly distributed within the structure. b) The elastic properties (i.e., E_{11}/E_b, E_{22}/E_b, ν_{12}, and ν_{12}) calculated for the RN unit cells using FE analysis. c) The deformation patterns of six RN unit cells under two loading conditions of $\varepsilon_{11} = 5\%$ and $\varepsilon_{22} = 5\%$ as predicted by FE analysis and observed in the mechanical tests on the 3D printed specimens. d) The network architecture of the trained unit cell elastic properties model, which maps the design of the unit cell to their elastic properties.

moderate positive and negative values of the Poisson's ratio as well as moderate values of the elastic moduli in both directions (Figure 1b). To validate the results of our simulations, we 3D printed and experimentally evaluated the elastic properties and deformation patterns of these six unit cells. The experimentally obtained values of the elastic moduli (see the stress–strain curves in Figure S4, Supporting Information) and Poisson's ratios show a good agreement with FE simulations (Table S4, Supporting Information). Moreover, the deformation patterns follow similar trends in both simulations and experiments (Figure 1c). In some elements within the FE models, we see higher levels of deformations predicted by FE models as compared to those observed experimentally. These small differences may be explained by the assumptions of the FE models, including a linear elastic constitutive behavior and fully fixed boundary conditions.

We trained a DL model, hereafter referred to as the "unit cell elastic properties model" that predicted the four elastic properties of any RN unit cell given its design (Figure 1d). Based on the results of our hyperparameter tuning pipeline, the applications of an undersampling process and a MinMaxScaler to the cross-validation (CV) data resulted in the best model performance. The hyperparameter tuning suggested a model with four hidden layers (500, 376, 252, and 128 hidden neurons in subsequent layers) without a regularization term, with Adam optimizer[39] and with ReLU activation functions throughout the layers (Table S5, Supporting Information). Within 200 epochs of model training with the optimized hyperparameters, the mean squared error (MSE) and the mean absolute error (MAE) reduced for the training dataset from 9.5×10^{-4} and 2.0×10^{-2} to 1.5×10^{-5} and 2.7×10^{-3}, respectively. For the validation dataset, the values of MSE and MAE reduced from 3.7×10^{-4} and 1.4×10^{-2} to 1.6×10^{-5} and 2.6×10^{-3}, respectively (Figure S6, Supporting Information). The evaluation of the trained model using the test dataset resulted in a coefficient of determination (R^2) of >0.993 and >0.999 for the Poisson's ratios and elastic moduli, respectively (Table S6 and Figure S7, Supporting Information). In general, the trained model exhibited a high degree of accuracy in predicting the elastic properties of the RN unit cells with an overall coefficient of determination (R^2) of 0.997, an MAE of 3.6×10^{-3}, and an MSE of 6.0×10^{-5} (Table S6 and Figure S7, Supporting Information). All these results show that the model is well trained without underfitting and overfitting and can, therefore, be further used for highly accurate, deterministic prediction of the elastic properties of various RN unit cell designs. The availability of such a model allows for the ultrafast prediction of the elastic properties associated with any design of RN unit cells with the evaluation of the DL model taking $\approx 2.44 \times 10^{-5}$ s per design (for prediction of 10^6 specimens), which is >20 times faster than the corresponding FE simulation.

2.2. Generative Inverse Design Framework

For the inverse design of RN unit cells, we trained a deep generative model based on CVAE that was paired with the pretrained forward predictor (i.e., the unit cell elastic properties model) (**Figure 2**a). Based on the results of the hyperparameter tuning, the size of the latent space was chosen to be 8. For both recognition and reconstruction models of the CVAE, we selected two hidden layers with 512 and 260 neurons, an Adam optimizer, and ReLU activation functions throughout both hidden layers. ReLU and Sigmoid were selected as the activation functions of the output layer for the recognition and reconstruction models, respectively (Table S7 and Figure S8, Supporting Information).

The reconstruction model of the trained CVAE was separated and called "unit cell generative model". To assess the generative ability of this model, the elastic properties of the test dataset and a random sampling from a normal distribution ($\varepsilon \approx N(0,1)$) were passed as inputs to this model. The predicted unit cell structures were passed as inputs to the unit cell elastic properties model and the predicted elastic properties were compared with the initially requested elastic properties of the test dataset. The results of this comparison showed an overall coefficient of determination (R^2) of 0.865, an MAE of 5.1×10^{-2}, and an MSE of 8.5×10^{-3} (Figure S9c and Table S8, Supporting Information). To assess the best achievable accuracy among the designs generated by the unit cell generative model, one hundred possible designs were generated for each set of elastic properties present in the test dataset. Then, the elastic properties of the generated unit cells were compared with the desired mechanical response provided to the model through the calculation of the regression metrics R^2, MSE, MAE, and root mean square error (RMSE). The best candidates were then selected among the 100 possible designs. Based on the proposed approach, the final evaluation of the unit cell generative model showed an overall R^2 of 0.977, an MAE of 1.2×10^{-2}, and an MSE of 3.0×10^{-4} (Figure S9d and Table S9, Supporting Information). In addition, the high accuracy of the unit cell generative model in generating new RN unit cells was demonstrated by comparing the DL-predicted elastic properties of the generated unit cells with their corresponding FE results (Figure S10, Supporting Information). Based on this comparison, R^2 of 0.98, 0.98, 0.99, and 0.99 were calculated for ν_{12}, ν_{21}, E_{11}, and E_{22}, respectively (Figure S10, Supporting Information).

2.3. Unit Cells with Requested Rare Elastic Properties

To demonstrate the generative ability of the unit cell generative model, grid-sampled values of double-auxetic elastic properties, which are rare occurrences in the natural sampling of RNs[21] were created and fed to the deep generative model. For each request, the elastic properties were defined as a combination of ν_{12} and ν_{21} in the range of (−1, −0.1) and an equal elastic modulus along both directions with values within the range of $E_{11}/E_b = E_{22}/E_b = (0, 0.25)$. For each input, the best design out of a 100 designs was selected. The four elastic properties of the generated unit cells predicted by the unit cell properties model are reported in a 3D scatterplot incorporating color coding for the fourth property (Figure 2b). To explore the expansion offered by the deep generative model over the observed elastic properties in the initial library (i.e., the training and test datasets), the existing elastic properties in the dataset and the nonduplicate values from the generative process were compared (Figure 2b). From the 3D scatterplot, we can see that the envelope of the achievable elastic properties is expanded in all three planes (i.e., planes of $\nu_{12} - \nu_{21}$, $E_{11}/E_b - \nu_{12}$, and $E_{11}/E_b - \nu_{21}$). The top view of the 3D scatterplot, which shows the expansion of the envelope in the $\nu_{12} - \nu_{21}$ plane, reveals the possibility of generating unit cells

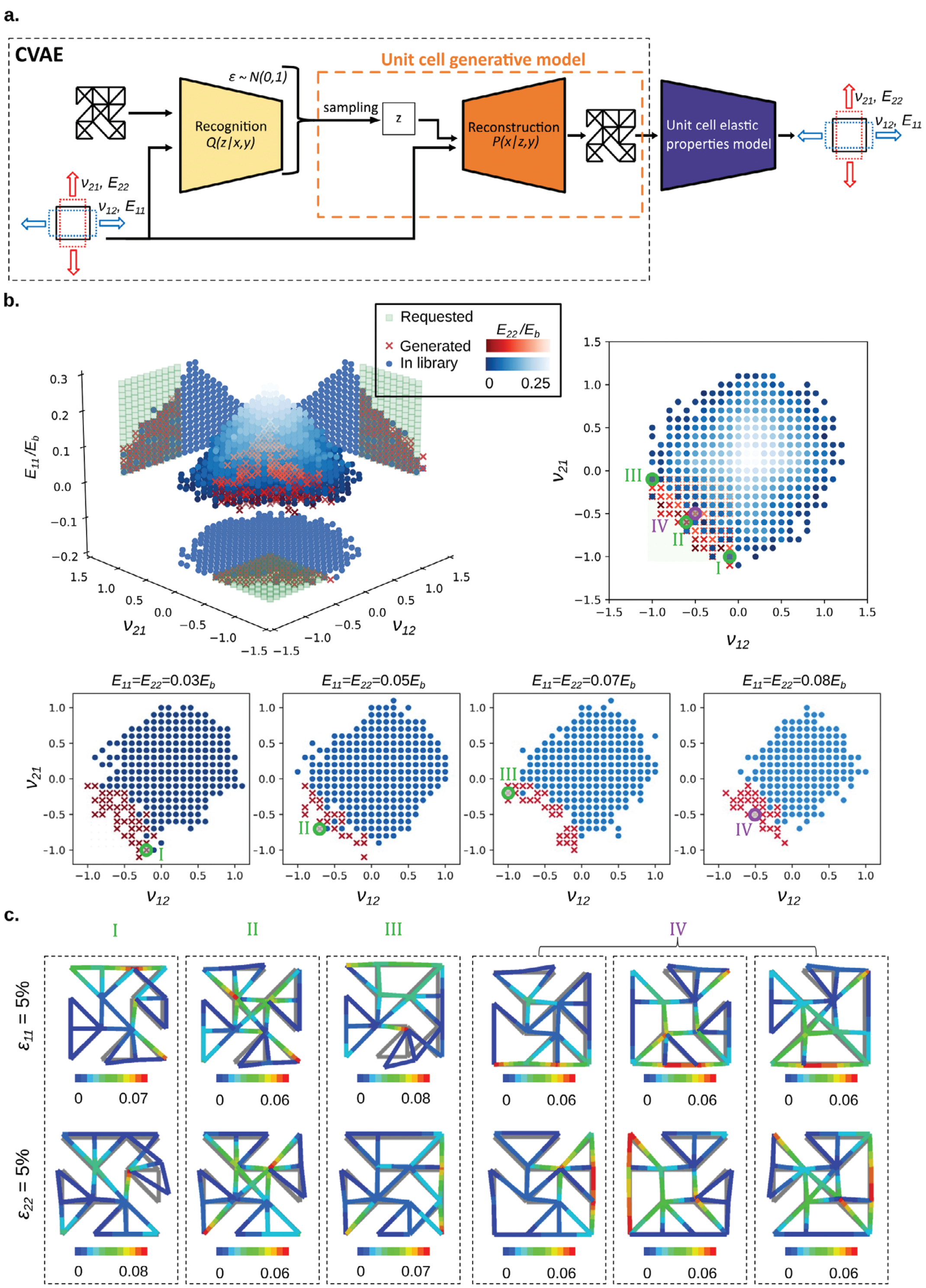

Figure 2. The unit cell generative model and its ability to generate new RN unit cells. a) The CVAE is composed of two parts: 1) the recognition part, which maps the unit cell design and its corresponding elastic properties to the latent space and 2) the reconstruction part, which converts a sampling of the latent space and the requested elastic properties to the corresponding design of the unit cell. The reconstruction part of CVAE is separated and is referred to as the "unit cell generative model" to generate RN unit cells given the target elastic properties. The elastic properties of the generated unit cells are further predicted by the unit cell elastic properties model for final filtering. b) A demonstration of the ability of the unit cell generative model to generate new unit cells with given elastic properties which were not present in the initial library. Cross-sections are presented to more clearly visualize the generated unit cells with new elastic properties. c) The deformation pattern of three specimens (i.e., I, II, III) with new elastic properties not present in the original library. Moreover, a group of specimens (i.e., IV) are presented to show the ability of the trained model to generate specimens with similar elastic properties.

with extreme double-auxetic properties (Figure 2b). In general, these results confirm the ability of the deep generative model to generate unit cells with new elastic properties that were not within the envelope of the elastic properties covered by the initial (i.e., training) library. The deep generative model is, therefore, of value for the efficient generation of unit cells with predefined elastic properties, especially rare-event properties, such as double-auxeticity.

As case studies, we selected four sets of elastic properties (I, II, III, and IV) with negative values of the Poisson's ratio and different Young's moduli (see the top views in Figure 2b) to illustrate the generated unit cells corresponding to these cases. For the elastic properties of case IV, three generated candidates are displayed to demonstrate the possibility of generating different designs exhibiting similar sets of elastic properties. The deformation patterns of these unit cells (when subjected to 5% strain along directions 1 and 2) were compared to the initial state of the generated unit cell (Figure 2c). The calculated error values averaged over the four components of the elastic properties were 8.3%, 8.6%, 3.6%, and 3.1% for unit cells I, II, III, and IV, respectively (Table S10, Supporting Information). These case studies show a high degree of accuracy of the deep generative model when used for the design of double-auxetic unit cells with elastic properties which were not seen before in the training or test datasets.

2.4. Elastic Properties of Combinatorial Designs

We studied combinatorial designs composed of $D_1 \times D_2$ repetitions of RN unit cells (**Figure 3**a). Assuming D_1 and D_2 are values varying in a range of (2, 20), we studied a total of 100 combinatorial designs from each RN unit cell. Based on a preliminary study we performed on the combinations of RN unit cells, we selected $D_1 = D_2 = 20$ as the maximum size of combinatorial designs due to the saturation of the elastic properties for larger numbers of unit cells (Figure S13, Supporting Information). We used the undersampled dataset of RN unit cells (dataset size = 81 569), which was used for the training of the unit cell elastic properties model, and performed numerical simulations for all the 100 combinatorial designs composed of these RN unit cells (size of dataset = 8 156 900). The generated dataset was further used to train a forward predictor called "size-agnostic model" that predicts the elastic properties of the combinatorial designs (Figure 3a).

To train the model, we assumed MinMaxScaler as the scaling method, ReLU as the activation function of all the hidden layers as well as of the output layer, and Adam as the optimizer with a learning rate of 0.0001, which were adopted from the hyperparameter tuning step of the unit cell elastic properties model. The hyperparameter tuning step of the deep generative model resulted in 6 hidden layers with 512, 428, 343, 258, 174, and 89 neurons, respectively (Table S11, Supporting Information). Within 200 epochs, the prediction errors (MSE, MAE) reduced from MSE $= 4.7 \times 10^{-3}$ and MAE $= 2.9 \times 10^{-2}$ to MSE $= 1.6 \times 10^{-5}$ and MAE $= 2.9 \times 10^{-3}$ for the training dataset and from MSE $= 4.1 \times 10^{-3}$ and MAE $= 1.4 \times 10^{-2}$ to MSE $= 1.7 \times 10^{-5}$ and MAE $= 3.0 \times 10^{-3}$ for the validation dataset (Figure S11, Supporting Information). The trained model had an overall R^2 of 0.995 for the test dataset (10% of the original dataset), confirming that it can accurately predict the elastic properties of the combinatorial designs (Table S12 and Figure S12, Supporting Information).

Combinatorial designs showed a wide range of elastic properties. The relative elastic moduli (E_{11}/E_b and E_{22}/E_b) and Poisson's ratios (ν_{12} and ν_{21}) calculated by the numerical simulations were in the ranges of (0, 0.3) and (−2, 3), respectively (Figure 3b). The 3D distribution of the elastic properties of the combinatorial designs resembled a square pyramid with inwardly curved faces whose base is placed within the $\nu_{12} - \nu_{21}$ plane. The distribution of the elastic properties in the $\nu_{12} - \nu_{21}$ plane was bounded by two hyperbolas, one with openings in the first and third quadrants and the other one with openings in the second and forth quadrants (Figure 3b).

To validate the results of our simulations, the elastic properties (Table S13, Supporting Information) and deformation patterns of four selected combinatorial designs were determined experimentally (Figure 3c). These specimens were selected with dimensions of $D_1 = D_2 = 4$ and exhibited a wide range of mechanical properties (Figure 3c; and Table S13, Supporting Information). These include a specimen with a positive Poisson's ratio in one direction and a zero Poisson's ratio in the other direction (specimen 1 in Figure 3c), a specimen with a negative Poisson's ratio in one direction and a zero Poisson's ratio in the other direction (specimen 2 in Figure 3c), an isotropic specimen with extreme elastic moduli in both directions (specimen 3 in Figure 3c), and an anisotropic specimen with a high elastic modulus in one direction and a low elastic modulus in another direction (specimen 4 in Figure 3c). We performed uniaxial tensile tests in two perpendicular directions (i.e., 1 and 2) on each of these specimens as well as digital image correlation (DIC) measurements for all specimens.

To study how the elastic properties vary with D_1 and D_2, we selected one of the RN unit cells and depicted the evolution of the four elastic properties as a function of changes in D_1. and D_2 (**Figure 4**a). We found a nonlinear relationship between the elastic properties and dimensions of the combinatorial designs of this unit cell that, as expected, saturates for large enough numbers of unit cells along each spatial direction (Figure 4a; and Figure S13, Supporting Information). For this elected RN unit cell, E_{11}/E_b, E_{22}/E_b, ν_{12}, and ν_{21} converge toward 0.046, 0.085, −0.04, and −0.2, respectively (Figure S13, Supporting Information). Another example is presented in Figure S14 (Supporting Information) in which E_{11}/E_b, E_{22}/E_b, ν_{12}, and ν_{21} converge toward 0.020, 0.048, 0.05, and 0.5, respectively. To validate the prediction results and to show the possibility of 3D printing of these specimens in different dimensions, we selected 3 combinatorial designs with dimensions of $D_1 = D_2 = 4$, $D_1 = 10$ and $D_2 = 4$, and $D_1 = D_2 = 10$. We performed uniaxial tensile tests in direction 2 on each of these specimens and compared their elastic moduli and Poisson's ratios with those of computational models. In addition, to show the possibility of achieving similar properties but in different dimensions, we selected four specimens with negative Poisson's ratio in direction 1 and $E_{11}/E_b = (0.01 \pm 0.01)/0.6$, $E_b = 0.6$ MPa (Figure 4b). We have performed DIC measurements for all specimens except of those that were very large (i.e., $D_1 = D_2 = 10$). This further analysis allowed us to compare the strain distributions within the structure. This comparison showed a good agreement between the local and overall

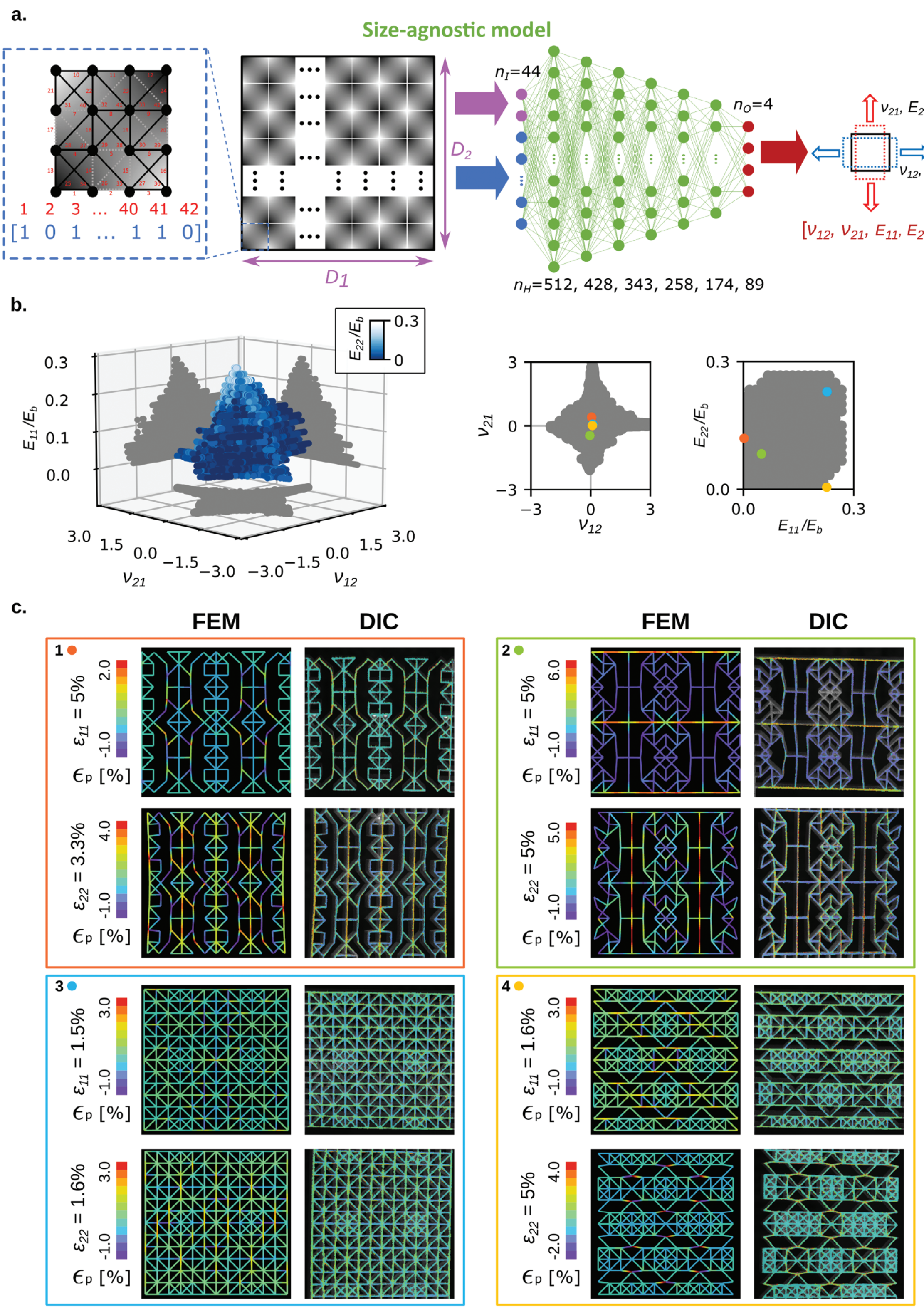

Figure 3. a) A schematic illustration and elastic properties of the combinatorial designs as well as the network architecture of the size-agnostic model. b) The envelope of the elastic properties achieved by the combinatorial designs, according to direct FE simulations. c) The deformation patterns of four combinatorial designs subjected to uniaxial tensile loading along two perpendicular directions (i.e., 1 and 2). The following loading conditions were used for most of the specimens: $\varepsilon_{11} = 5\%$ and $\varepsilon_{22} = 5\%$. For specimens with very high elastic moduli smaller applied strains were used. Both the results of FE analysis and DIC experimental results obtained using mechanical tests on the 3D printed specimens are presented. The comparison between FE simulations and experimental results is provided in Table S13 (Supporting Information).

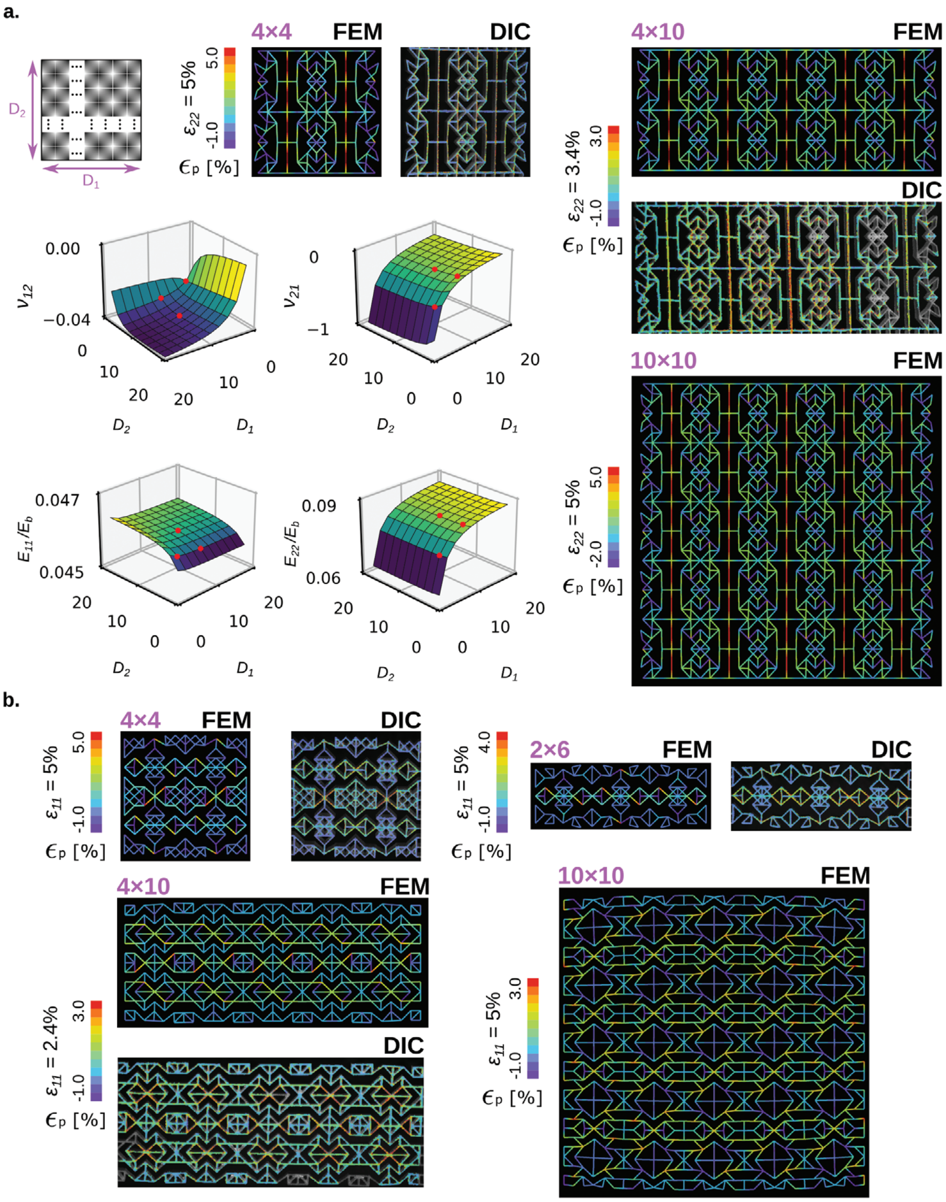

Figure 4. a) The evolution of the elastic properties as functions of D_1 and D_2 for a specific case study. Each combinatorial design with a given dimension ($D_1 \times D_2$) is created by repeat filliping a specific RN unit cell D_1 times vertically (along direction 1) and D_2 times horizontally (along direction 2). The vectors containing D_1 and D_2 the binary vectors representing the design of the unit cells are introduced to the size-agnostic model as input. The model then returns the predicted elastic properties of the combinatorial design as output. The deformation patterns of one lattice at different sizes (i.e., 4 × 4, 4 × 10, 10 × 10) subjected to the following loading conditions: $\varepsilon_{22} = 5\%$, $\varepsilon_{22} = 3.4\%$, and $\varepsilon_{22} = 5\%$, respectively. Both the results of FE analysis and DIC measurements obtained from the mechanical tests of the 3D printed specimens are presented. It was not possible to perform DIC for the 10 × 10 combinatorial design due to its large dimensions, but the deformation pattern of this specimen subjected to $\varepsilon_{22} = 3\%$ is shown in Figure S15 (Supporting Information). b) The deformation patterns of four representing designs in different dimensions (i.e., 4 × 4, 2 × 6, 4 × 10, and 10 × 10) subjected to the following loading conditions: $\varepsilon_{11} = 5\%$, $\varepsilon_{11} = 5\%$, $\varepsilon_{11} = 2.4\%$, and $\varepsilon_{11} = 5\%$, respectively, showing similar rare properties (i.e., negative Poisson's ratio and $E_{11}/E_b = (0.01 \pm 0.01)/0.6$, $E_b = 0.6$ MPa) while their overall dimensions are different. Both the FE results and DIC measurements obtained from mechanical tests on the 3D printed specimens are presented. It was not possible to perform DIC for the 10 × 10 combinatorial design due to its large dimensions, but the deformation pattern of this specimen subjected to $\varepsilon_{11} = 5\%$ loading condition is shown in Figure S16 (Supporting Information). The comparison between FE simulations and experimental results is provided in Table S14 (Supporting Information).

deformation withing the structure (Figure 4a,b), as well as the measured mechanical properties that were obtained numerically and experimentally (Table S14, Supporting Information). The mechanical tests of these specimens indicated that the deformation patterns follow the same trends as observed in the simulations. The mismatches between the simulations and mechanical tests can be attributed to the assumptions used in the simulations (e.g., a linear elastic constitutive equation), differences between the experimental and simulated boundary conditions, and manufacturing imperfections.

2.5. Inverse Design of Lattice Structures with Requested Elastic Properties and Dimensions

We combined the unit cell generative model and the size-agnostic model to develop a comprehensive and powerful framework called Deep-DRAM, which can inversely design lattice structures with given elastic properties and dimensions. Given the requested elastic properties, we first used the deep generative model to generate 10^5 RN unit cells. It takes the deep generative model 5.7 ± 0.1 s on a workstation (see the Experimental Section for the specifications) to generate these unit cells. Since the returned unit cell structures would vary in their design and mechanical response, they can deviate from the requested set of elastic properties. This is, in fact, an advantage of such a generative model because the actual elastic properties of a lattice structure with a finite (anisotropic) number of unit cells along each spatial direction may be quite different from the unit cell properties. The presence of such natural variations in the elastic properties of the generated unit cells enables us to feed a large number of designs created by the deep generative model to the size-agnostic model that is trained to account for the effects of size along each direction. Then, all these generated unit cells together with the desired dimensions are introduced to the size-agnostic model to predict the elastic properties of these combinatorial designs. Finally, the MSE values showing the difference between the target properties and the final elastic properties of the generated combinatorial designs are calculated. Based on the error values, we selected the designs that best matched the target elastic properties for the given dimensions (**Figure** 5a).

To demonstrate the functionality of Deep-DRAM, we assumed a constant value for the elastic modulus (i.e., $E_{11}/E_\mathrm{b} = E_{22}/E_\mathrm{b} = 0.03$) and a range of (−1, 1.6) for the Poisson's ratios with a step size of 0.2 (i.e., 14 groups of values for the Poisson's ratios). In total, we studied 196 (i.e., 14 × 14) sets of elastic properties. We also predefined a dimension of $D_1 = D_2 = 4$ for the generated combinatorial designs. Using these predefined values, 1.96×10^7 combinatorial designs were generated and filtered based on their MSE values. The whole design procedure including the inverse design of the RN unit cells, combining the unit cells into combinatorial designs, prediction of the elastic properties of the combinatorial designs, and finding the best candidates based on the calculated MSE values took ≈38 min (for all the 1.96×10^7 designs) using the same, above-described computer. A few examples of generated RN lattice structures with predefined elastic properties and dimensions are presented in Movie S1 (Supporting Information) (RN lattice structures with negative Poisson's ratio) and Movie S2 (Supporting Information) (RN lattice structures with positive Poisson's ratio).

To quantify the expected error values for the design of combinatorial designs with different elastic properties and dimensions, we repeated the aforementioned procedure for 196 selected sets of elastic properties considering two groups of dimensions. In the first group, we predefined equal dimensions (i.e., $D_1 = D_2 = [2, 4, 6, 8, 10, 12, 14, 16, 18, 20]$), while in the second group we assumed $D_2 = 2$ and $D_1 = [2, 4, 6, 8, 10, 12, 14, 16, 18, 20]$. We defined the envelope of successful designs such that it was bounded by the designs corresponding to an MSE value of 0.1. The heat maps of the MSE values depict the expected error values for generating combinatorial designs when the elastic properties and dimensions are provided as input (Figure 5b). The gray regions represent the designs whose elastic properties are associated with MSE values exceeding the acceptance threshold (Figure 5b). Upon closer inspection, we found that the gray regions primarily correspond to the property–size combinations that simply cannot arise from the considered RN. As expected, the envelopes of successful design generations converge for large enough values of D_1 and D_2 (Figure 5b). For larger sizes, the heat maps of MSE values for combinatorial designs with $D_1 = D_2$ are symmetrical around the $\nu_{12} = \nu_{21}$ line. This increased symmetry indicates a more isotropic behavior of RN combinatorial designs as their dimensions increase. In the other group of the combinatorial designs with $D_2 = 2$ and varying D_1 values, we do not expect isotropy because the ratio of D_1/D_2 increases and the geometry is not symmetric anymore.

2.6. Stress Distribution

Deep-DRAM provides many solutions to the design problem of finding RN lattice structures with predefined dimensions and elastic properties. It is, therefore, possible to apply additional design requirements, such as criteria regarding the stress distributions observed within the generated structures under various types of loading conditions. One such criterion is to choose the design with the minimum peak stress, thereby enhancing their resistance against fatigue and failure. To demonstrate the utility of our size-agnostic inverse design framework within this context, we first generated combinatorial designs with predefined elastic properties and dimensions. We then filtered the generated designs based on their maximum von Mises stress (**Figure** 6a) (see Movie S3, Supporting Information). As representative cases, we studied three groups of combinatorial designs with predefined specifications: i) $D_1 = D_2 = 4$, $\nu_{12} = -0.2$, and $\nu_{21} = 0.2$, ii) $D_1 = 10$, $D_2 = 4$, $\nu_{12} = \nu_{21} = 0.5$, and iii) $D_1 = D_2 = 10$, $\nu_{12} = \nu_{21} = -0.2$, while the elastic modulus was assumed to be the same for these three groups (i.e., $E_{11}/E_\mathrm{b} = E_{22}/E_\mathrm{b} = 0.03$). From each group, the first 1000 designs with MSE < 0.1 were further analyzed using FE simulations to determine the stress distribution within their elements under two loading conditions (i.e., $\varepsilon_{11} = 5\%$ or $\varepsilon_{22} = 5\%$). The normalized peak values of the von Mises stress in directions 1 and 2 were then calculated (Figure 6b). From each group, we selected two specimens with almost the same MSE but with either the minimum or maximum Euclidean distance from the origin. The stress distributions corresponding to these case studies clearly show stress concentrations in some regions within the specimens with the maximum Euclidean distances (i.e., specimens 2, 4, and 6), while the stress distribution are comparatively more uniform within specimens 1, 3, and 5 (Figure 6c,d). The specimens with high peak stresses are prone to premature crack initiation and growth and should be avoided in the design of mechanical metamaterials aimed for practical applications. Further analysis of these results shows 310%, 250%, and 270% difference between the maximum and minimum values of the von Mises stresses of the three study groups, which are very substantial numbers within the context of peak stress reduction analysis.

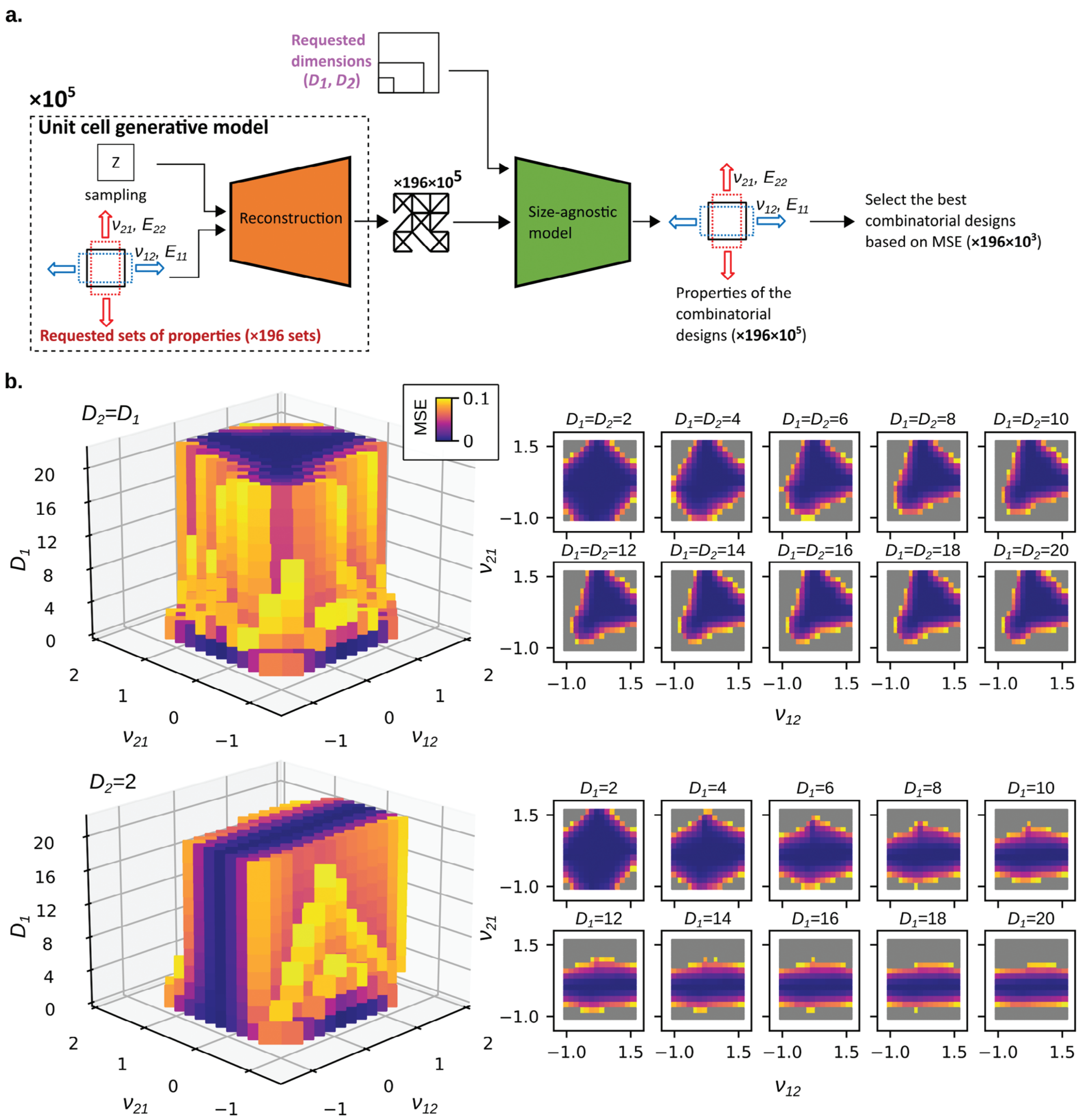

Figure 5. The structure of Deep-DRAM as a size-agnostic inverse design framework. a) In this framework, the deep generative model and the size-agnostic model are combined to generate combinatorial designs with desired elastic properties and dimensions. The best candidates among the generated combinatorial designs are then selected based on their MSE values. b) The heat maps of the MSE values indicating the expected error values for generating combinatorial designs with predefined elastic properties and dimensions.

2.7. Exotic Properties and their Recurring Features

We utilized our models to develop lattices with rare mechanical properties (i.e., double-auxeticity). Such deployment allowed us to tackle the common challenge of obtaining structures with such exotic properties[21] demonstrating how ML-based methods help bridging problems in the design space of metamaterials. Moreover, by generating a large number of designs, we studied the main features that determine such properties, and laid two different hypotheses of their significance. If a single "dominant" structure with similar exotic properties emerged from the analysis, a design template for future optimization processes could emerge as a result. If, in contrast, no "dominant" structure emerges, this study would demonstrate that ML-based

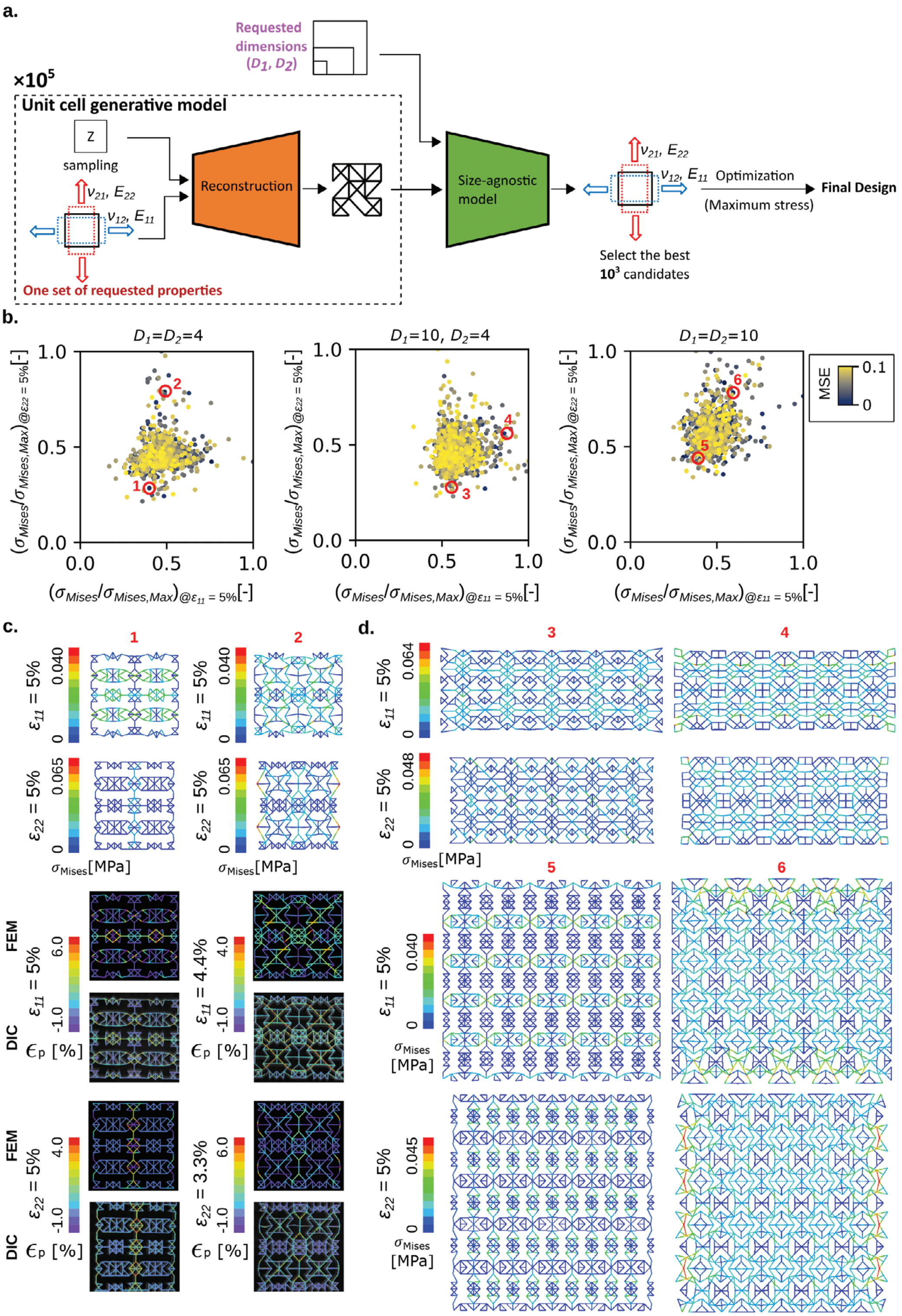

Figure 6. Multiobjective design where the minimization of peak von Mises stresses is considered as an additional design requirement. a) Finding the optimized combinatorial designs based on the stress values of the elements of the lattice structure (see Movie S3, Supporting Information). b) As representative cases, combinatorial designs of three groups (i.e., $D_1 = D_2 = 4$, $D_1 = 10$, and $D_2 = 4$, and $D_1 = D_2 = 10$) were studied. For each group, the first 1000 generated combinatorial designs with *MSE* values below 0.1 were further analyzed using FE simulations to determine the stress distributions within their elements. The normalized peak von Mises stresses when the structure was subjected to a strain of $\varepsilon_{11} = 5\%$ are plotted against the same type of stress when the applied stain is $\varepsilon_{22} = 5\%$. c,d) The deformation patterns and stress distributions of the elements of some selected combinatorial designs. For the specimens in (c) further DIC measurement was performed and the comparison of strain distribution between FE and DIC are shown in four bottom rows in (c).

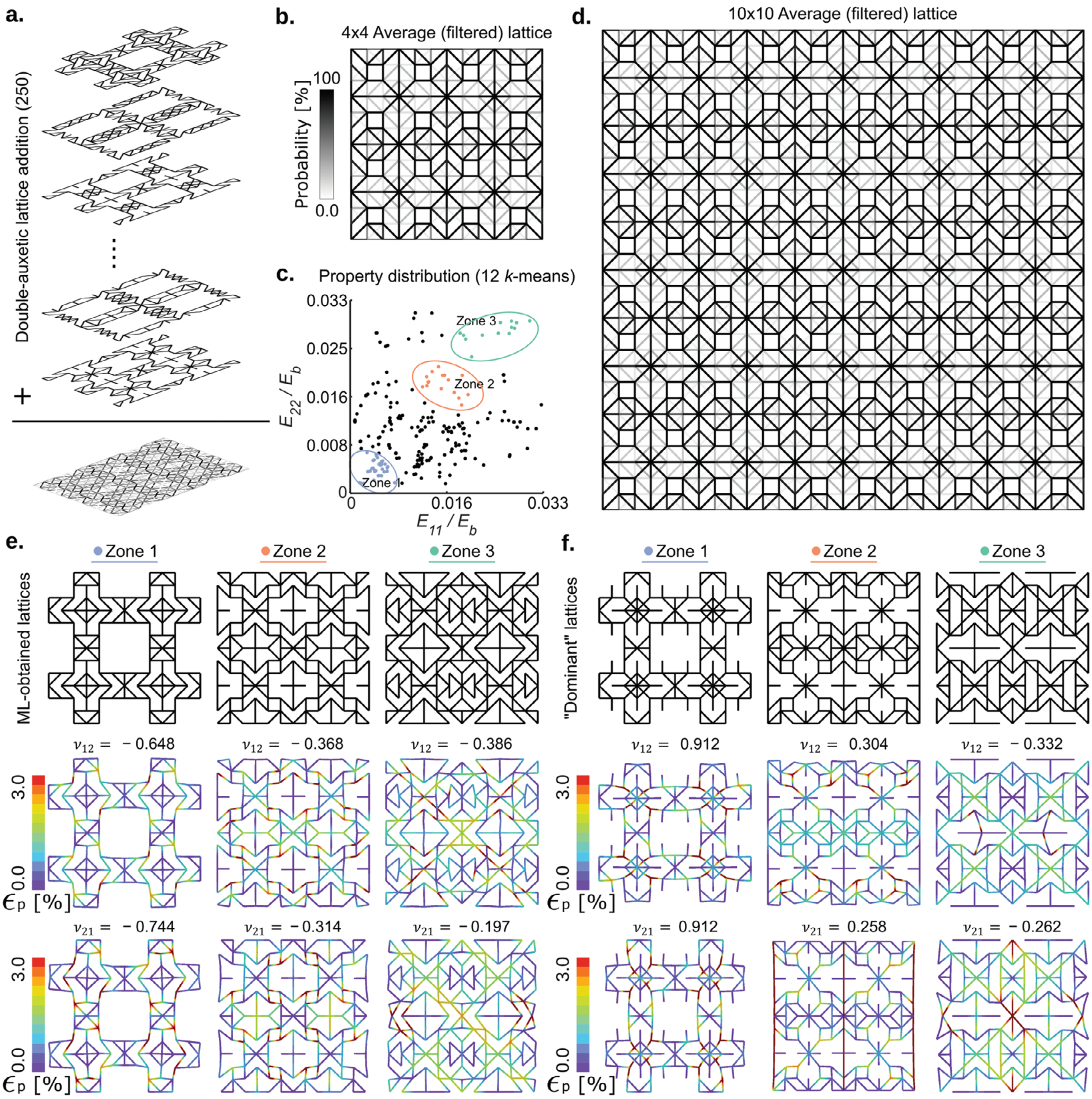

Figure 7. The recurring features of double-auxetic designs (i.e., $\nu_{12} = -0.4 \pm 0.1$ and $\nu_{21} = -0.4 \pm 0.1$). a) The process of obtaining the "dominant" features for such properties, where probability maps were calculated using 250 different designs. b) The probability maps of the 4 × 4 unit cell lattices. c) The distribution of the elastic moduli of these designs that fall in the ranges $E_{11}/E_b = (0.01 \pm 0.01)/0.6$ and $E_{22}/E_b = (0.01 \pm 0.01)/0.6$, with E_b = 0.6 MPa, and include compliant (zone 1), medium (zone 2), and stiff (zone 3) lattice structures. b,d) The filtered equivalents of the 4 × 4 (b) and 10 × 10 (d) unit cell lattices were obtained to showcase the similarities of the probability maps regardless of the lattice size. e) Representative examples of ML-obtained designs with double-auxeticity but different stiffness moduli corresponding to different zones (top-row) tested in direction 1 (middle-row) and direction 2 (bottom-row). f) The resulting behavior of the different "dominant" structures corresponding to different zones with different elastic moduli (top-row) tested in direction 1 (middle-row) and direction 2 (bottom-row).

methods are fundamental to obtain the plethora of design possibilities that result in such properties. Thus, to discover such "dominant" structures, we generated 250 new geometries for materials with specific target properties (i.e., $\nu_{12} = -0.4 \pm 0.1$, $\nu_{21} = -0.4 \pm 0.1$, $E_{11}/E_b = (0.01 \pm 0.01)/0.6$ and $E_{22}/E_b = (0.01 \pm 0.01)/0.6$, with $E_b = 0.6$ MPa (**Figure 7**). These simulations were conducted across two different material sizes (i.e., 4 × 4, and 10 × 10 unit cells) (Figure 7b,d). We also categorized the resultant elastic moduli into three main groups of low (zone 1), medium (zone 2), and high (zone 3) elastic moduli (Figure 7c). The representative lattice structures of ML-obtained designs show similar double-auxetic properties as requested (Figure 7e). The microstructures of these representative structures were, however, significantly different in each zone, highlighting complementary microstructures when comparing structures with compliant or stiff elastic moduli (Figure 7e).

In order to find out the recurring features in each zone, we further organized struts based on their probability of occurrence, from the highest to the lowest. Additional struts were sequentially added to the structure until the total number equaled the mean count of struts per design, as observed in pre-existing strut configurations. Structures classified as "dominant" were identified via the application of thresholding techniques to their respective probability distribution maps in each zone (Figure 7f). These threshold values were reverse-engineered to align the resultant number of beams with the mean number of struts per lattice, specific to each zone.

These results demonstrate that our ML-model can identify a wide range of viable structures, thereby increasing the likelihood of discovering metamaterials with unprecedented properties. It also suggests that combining features from these dominant structures could lead to new materials that may, individually, not meet all the desired criteria (Figure 7e,f).

Moreover, ML-obtained designs with double auxetic properties show unique features depending on their level of elastic moduli (Figure 7e). These unique features individually give rise to the desired combinations of rare properties while, they are not collectively pointing toward a specific dominant pattern of features (Figure 7f), implying that a thorough exploration of as many designs as possible is required to discover such specific and unique features.

3. Discussions and Future Outlook

The Deep-DRAM framework presented here is a combination of four modules and provides many opportunities for the design of mechanical metamaterials for practical use in the design of advanced functional devices. In addition, the presented modular approach allows the individual modules to be combined with other tools available elsewhere to provide solutions for the many challenges encountered in the design of designer materials. To a degree, the modularity of this approach and the probabilistic nature of the CVAE allows us to decouple some of the problems encountered in the design and optimization of mechanical metamaterials, thereby enabling multiobjective design optimization with minimum development and computational costs. For example, the multiple objectives of achieving a certain set of elastic properties and minimizing the peak stress within the structure can be handled in-series with minimum computational costs. That is partially due to the extremely high speeds of both generating and evaluating individual designs, which are in the range of microseconds.

In conventional computational design approaches, including FE analysis, topology optimization, gradient-based optimization, genetic algorithms, and response surface methodology, inverse problems often result in degenerate designs, meaning that multiple structural configurations could yield an identical set of material properties. The risk of degeneracy is particularly evident when parameters, such as elastic properties and dimensions are given a priori. Without the ability to distinguish between nearly identical outcomes, conventional methods may fall short in their predictive capability.[40,41]

Deep-DRAM could address these issues by employing an auxiliary objective function aimed at minimizing degeneracy in the generated unit cells. For instance, introducing a regularization term in the loss function that penalizes similar structural features could prevent the model from converging to degenerate solutions. This aspect becomes particularly salient when the model is aimed at designing structures under multiple physical constraints where degenerate designs can have differing performance metrics.

The integration of a DL-based forward predictor model with a deep generative model, such as the CVAE, serves multiple critical functions in the framework for designing RN unit cells. The forward predictor not only validates the unit cell designs generated by the CVAE, ensuring their alignment with predefined elastic properties, but also provides a rapid and computationally efficient evaluation mechanism. This efficiency is particularly advantageous when compared to traditional, computationally intensive methods, such as FE analysis, thereby facilitating a more rapid iteration process in the design cycle. Additionally, the forward predictor enhances the robustness of the overall system, serving as a reliability check against overfitting by the generative model. The forward predictor's ability to quickly validate the elastic properties of generated designs ensures the suitability of the framework for generating complex, application-specific lattice structures. Overall, the DL-based forward predictor is an indispensable component in this generative inverse design framework, contributing not just to validation but also to computational efficiency and robustness.

The integration of the Kullback–Leibler (KL) divergence term in the loss function serves an important role in shaping the latent space within the CVAE framework. By incorporating KL divergence, the model fosters a more compact and structured latent space. This not only facilitates effective encoding but also ensures generalizability, which is crucial for material design applications. The KL term acts as a regularization mechanism, imposing penalties for deviations from a predefined probabilistic distribution. This optimization refines the latent space, leading to more reliable and interpretable representations of mechanical properties in metamaterials.

In the present study, we have primarily focused on the use of CVAEs for the forward modeling of mechanical properties in metamaterials. However, the use of graph neural networks (GNNs) presents an intriguing avenue for future investigations, particularly given the intricate graph-like relationships between constituent elements in architected materials. Previous studies[42–44] have already demonstrated the applicability of GNNs in capturing the complex topologies and spatial dependencies in such materials. Specifically, GNNs can provide a more direct encoding of the material's microarchitecture, given their ability to directly model the relationships between adjacent elements in a complex network. Future work may explore the potential of integrating GNNs into the current framework with the anticipation that this could further refine the model's predictive accuracy and generalizability.

In the context of machine learning applications, particularly in the identification of unit cells with rare mechanical properties, various distribution scenarios emerge that require careful investigations—namely, in-distribution (ID), near-out-of-distribution (NOD), and out-of-distribution (OOD). The current study deploys Deep-DRAM, a modular, DL-oriented framework, to address the size-agnostic inverse design problem. Experimental evaluations suggest that the model exhibits commendable performance in predicting and inverse designing within ID and NOD contexts, adhering to the well-established practices where test datasets incorporate elements distinct from the training set. Nevertheless, a characteristic limitation pertaining to OOD scenarios has been observed—a phenomenon corroborated by existing literature on the constraints of neural networks as high-dimensional function estimators.[45,46]

While Deep-DRAM has been formulated to generate structures with mechanical properties that are intrinsically OOD, especially upon specific requests for extreme properties, the model does manifest a capacity of producing samples beyond the training distribution, hence showcasing its adaptability to OOD demands. This serves as a direction for future investigations into the model's resilience against OOD inputs, a particularly important point given the study's focus on rare mechanical properties. Within the modular architecture of Deep-DRAM, individual components—from the DL-based forward predictor model for anisotropic properties to the generative model predicated on CVAEs—warrant further evaluation. Methodologically, resilience against OOD inputs can be examined via robust techniques, such as CV,[47,48] bootstrapping,[49,50] or Bayesian methods for uncertainty quantification.[51–54] It would be insightful to synthetically generate pseudo-out-of-distribution samples to simulate conditions or properties not initially covered in the training set. Employing metrics, such as the coefficient of determination (i.e., R^2), MAE, and RMSE, could serve as effective tools for evaluating the model's predictive fidelity under these nuanced conditions.

In future research, it may be valuable to investigate the use of encoded latent representations[55–58] from the bottleneck of the VAE to more efficiently solve regression problems. The premise is that initially encoding a microstructure using the encoder part of the VAE could potentially minimize the number of parameters needed for forward models. Importantly, this approach may lead to models that generalize better across different tasks and conditions.

The manufacturability constraints are pivotal to the utility of DL-generated mechanical metamaterials. In the current study, selective laser sintering (SLS) method was employed to fabricate 2.5D metamaterials. However, this technique has two notable limitations: the size of the build plate and a minimum feature size of 700 µm. The former restricts the creation of structures to dimensions no greater than 190 mm × 190 mm (the maximum dimensions that can fit are 10 × 10 unit cells that were scaled by 80%), while the latter impedes downscaling, as the strut thickness in the metamaterial can fall below the resolution capabilities of the printer. These limitations necessitate the exploration of alternative techniques, such as stereolithography (SLA) or two-photon polymerization (2PP), for achieving finer resolutions in the fabrication of micro- or submicroscopic metamaterials.[59–61] Future research could integrate these manufacturing constraints into DL models to ensure the practical feasibility of computationally designed structures.

There are a number of points that need to be discussed regarding the broader use of Deep-DRAM. First, while we focused on a specific choice of RN for this study, the same methodology can also be used for any underlying design paradigm including any other types (i.e., size, organization) of random structures as well as ordered structures and a combination thereof. Second, the modular design of our approach as well as its ad hoc combination with direct FE modeling affords it a high degree of flexibility in terms of taking design requirements into account and tackling multiple types of problems that are challenging in their own right. For example, the problem of finding rare combinations of elastic properties is treated independently in multiple other studies[14,19] but can also be studied, within the confines of the selected RN design, using the modules developed here. Third, our focus on the linear elastic properties meant that we used linear elastic constitutive models everywhere in the current study. However, the same approach can be used to study the nonlinear properties of RN designs or to consider any other aspects of their constitutive behavior (e.g., viscoelasticity). The only difference would be that the FE models need to be modified to reflect the more complex constitutive behavior. Indeed, the relative advantage of the presented approach would be even more evident when the simulation time is longer, such as the case of nonlinear or viscoelastic constitutive behaviors. Fourth, the compact and computationally efficient nature of the final models means that they can be implemented in low-resource settings to power edge computing[62,63] applications. Finally, some elements of the developed modulus (i.e., even individual layers) can be used for more advanced machine learning approaches, such as transfer learning, to further generalize the domain of application of our models.

4. Conclusions

We have developed a size-agnostic inverse design framework, Deep-DRAM, which can generate RN lattice structures not only with predefined elastic properties but also with predefined dimensions suitable for any intended application. We showed that combining deep generative models with forward predictors is successful in generating bespoke mechanical metamaterials while also satisfying additional design requirements, such as minimum peak stresses, to improve the endurance of designer materials for real-world applications.

5. Experimental Section

We studied restricted RN unit cells in which the nodal points of the beam-like elements were fixed at specific locations. The design of these unit cells was inspired by the previous research[21] that computationally explored the auxeticity and stiffness of RNs and demonstrated a wide range of elastic moduli and Poisson's ratios for this type of mechanical metamaterials. For this work, RN unit cells composed of different node numbers (i.e., $n_x = n_y = 3, 4, 5, 6, 7$, and 8) are first studied to find out the least number of nodes that corresponds to the broadest range of elastic properties. It is assumed the internodal distances of Δx and Δy in directions 1 and 2, respectively. The overall size of a unit cell is, therefore, given by: $L \times W$ ($L = n_y \times \Delta y$ and $W = n_x \times \Delta x$) (Figure 1a). Also, the in-plane ($t = 1$ mm) and out-of-plane ($T = 10$ mm) thicknesses for the RN unit cells was assumed. The beam-like elements were randomly distributed to connect the whole grid. Unit cells with the network connectivity values of $Z_g = 2.5, 3, 3.5, 4$, and 4.5 (Figure 1a) were studied. Further combinatorial designs that are composed of different numbers of rows and columns of RN unit cells were studied.

Computational Models: All the FE models were created using MATLAB (MATLAB R2018b, MathWorks, USA) codes. Custom codes were used to design the structures by randomly connecting each node to its surrounding nodes and to perform the FE simulations that estimate the elastic properties of the resulting structures (i.e., the elastic moduli and Poisson's ratios in both orthogonal in-plane directions). The random distribution of beams resulted in "loose designs" where some nodes were not connected to the overall grid. To exclude such designs, a graph-based search method (breadth-first search[64]) for filtering and discarding such invalid unit cell designs was used. The applied graph-based algorithm sped up the process by nearly 900 times as compared to an image-based filtering method used previously[21] (more information is provided in Figure S1, Supporting Information). The codes were further extended to incorporate the RN unit cells into the combinatorial designs (Figure 3a).

The three-node quadratic beam elements (Timoshenko beam elements) with rectangular cross-sections ($t \times T$) and with two translational (i.e., u_{11} and u_{22}) and one rotational (i.e., u_{33}) degrees of freedom (DOF) at each node were employed. An elastic material with a Young's modulus of $E_b = 0.6$ MPa and a Poisson's ratio of $\nu_b = 0.3$ was then assigned to elements. For each structure, two FE models were created to separately apply a strain of 5% along 1- and 2-directions. In the first model, the top nodes were subjected to a strain of 5% along the 2-direction ($u_{11} = u_{33} = 0$ and $u_{22} = 0.05 \times L$), while all the DOF of the bottom nodes were constrained ($u_{11} = u_{22} = u_{33} = 0$). In the second model, the right nodes were subjected to 5% strain along the 1-direction ($u_{22} = u_{33} = 0$ and $u_{11} = 0.05 \times W$) while all the DOF of the left nodes were constrained ($u_{11} = u_{22} = u_{33} = 0$). More information about the FE equations used for the numerical simulations are provided in the Supporting Information.

To calculate the elastic moduli of the structures ($E_{11} = \sigma_{11}/\varepsilon_{11}$ and $E_{22} = \sigma_{22}/\varepsilon_{22}$), the normal stresses along directions 1 and 2 ($\sigma_{11} = \overline{F_{11}}/(L \times T)$, $\sigma_{22} = \overline{F_2}/(W \times T)$ (Figure 1a)) were divided by the strain applied along the same direction ($\varepsilon_{11} = \varepsilon_{22} = 5\%$). In these equations, $\bar{F}_{11}$ and $\bar{F}_{22}$ are the mean reaction forces along directions 1 and 2 at the right and top nodes, respectively ($\overline{F_{11}} = (\sum_{i=1}^{n_R} F_{11,i})/n_R$, $\overline{F_{22}} = (\sum_{i=1}^{n_T} F_{22,i})/n_T$, where n_R and n_T are the total numbers of the right and top nodes, while $F_{11,i}$ and $F_{22,i}$ are the reaction forces along directions 1 and 2 at each of the right and top nodes, respectively). The transverse strain as the ratio of the average displacement of the lateral nodes was then calculated to the initial transversal length of the structure (in the case of $\varepsilon_{axial} = \varepsilon_{11} = 5\%$: $\varepsilon_{trans} = \varepsilon_{22} = (\sum_{i=1}^{n_T} \delta y_i)/(L \times n_T)$, and in the case of $\varepsilon_{axial} = \varepsilon_{22} = 5\%$: $\varepsilon_{trans} = \varepsilon_{11} = (\sum_{i=1}^{n_R} \delta x_i)/(W \times n_R)$). The transverse strain was then divided by the applied axial strain to calculate the Poisson's ratio ($\nu = -\varepsilon_{trans}/\varepsilon_{axial}$).

Deep Learning—Unit Cell Elastic Properties Model: A predictor model was trained that was referred to as the "unit cell elastic properties model" which aims to learn the mapping from the space of RN unit cell designs to that of their elastic properties. This model takes as input a binary vector representing the RN unit cells (i.e., a binary vector of 0 and 1 values, where 1 indicates the presence of an element and 0 indicates its absence) and returns the elastic properties (E_{11}, E_{22}, ν_{12}, and ν_{21}) of the unit cells as output. Before training the model, an initial data analysis process followed by a hyperparameter tuning study was performed. To select the options and parameters for both data analysis and hyperparameter tuning, a pipeline training technique (Figure S5, Supporting Information) which combined data analysis options and model hyperparameters in its search space was used. Pipeline training automates the training process including data analysis and hyperparamater tuning and optimizes the model considering different configurations of the parameters of the search space of the pipeline.

A workstation (CPU = Intel Xeon W-2295, RAM = 256 GB) and a Python script (Python 3.9.7) to tune the parameters of the pipeline's search space was used. Though this, 10 368 combinations of parameters were investigated (Table S5, Supporting Information) and the best pipeline parameters were selected. For data analysis, data resampling and data scaling were selected to be investigated since the size and distribution of both inputs and outputs are important for the success of the model training step. As for the model hyperparamaters, the parameters were selected describing the design of the DL models (i.e., the width and depth of the hidden layers as well as the trend of the variation of the number of hidden neurons per layer), the regularization terms, the type of the optimizer algorithm, the activation functions of the hidden layers and output layer, and the application of batch normalization. The search methods of CV grid search from scikit-learn (version 1.1.1) was used to systematically iterate over the predefined values of the search space parameters (see the Supporting Information for a more in-depth discussion of the methods).

The overall performance of the model was assessed by characterizing its ability to generalize from the training dataset to the test dataset to avoid both under- and overfitting. To avoid overfitting, *k*-fold CV was used that divides the training dataset into *k* smaller sets. Threefold CV, meaning that each set equals 33% of the training dataset was used. Note that 10% of the overall dataset was kept as the test dataset for final model evaluation.

MSE was selected (Equation (1)) as the loss function of the model to ensure the regression line changes only slightly for a modest change in the data point. For the evaluation of the model training, the coefficient of determination (R^2) (Equation (2)) was used which indicates the amount of target variance explained by the model's independent variables

$$\mathrm{MSE} = \frac{1}{n}\sum_{i=1}^{n}\left(y_i - \widehat{y}_i\right)^2 \tag{1}$$

$$R^2 = 1 - \frac{\sum_{i=1}^{n}\left(y_i - \widehat{y}_i\right)^2}{\sum_{i=1}^{n}\left(y_i - \bar{y}\right)^2} \tag{2}$$

where n is the size of the dataset, y_i is the *i*th real target, $\widehat{y}_i$ is the corresponding predicted value, and $\bar{y}$ is the mean value of y ($\bar{y} = \frac{1}{n}\sum_{i=1}^{n} y_i$).

Deep Learning—Deep Generative Model: A deep generative model was trained that allows for the inverse design of RN unit cells. This model is based on CVAE and follows a similar approach as in a number of previous studies.[26,65] The key difference between CVAE and VAE is that CVAE can incorporate certain conditions in the training process.[65,66] Here, the additional conditions concern the elastic properties of the RN unit cells. Two deep neural networks were utilized as the submodels of the CVAE, each with a structure purposefully built for their specialized roles. More specifically, they are a recognition network and a reconstruction network which are coupled in an encoder-decoder format (Figure 2a). The recognition model transfers the designs of the RN unit cells as well as their corresponding elastic properties into a low-dimensional, continuous, and ordered latent space[27] The reconstruction model uses the four elastic properties and the latent variables to recreate the binary vector representing the metamaterial design. After the successful training of the CVAE, the reconstruction model was separated and used as the deep generative model. The input to this deep generative model was the desired elastic properties of the RN unit cell as well as a random sampling from a normal distribution with the same dimensions as the latent space.

The loss function that was utilized to train the CVAE ($\mathcal{L}_{CVAE}$) was obtained from the loss function of a standard VAE ($\mathcal{L}_{VAE}$) with conditional information included. The loss function of VAE consists of two terms, the reconstruction error and the KL term, and is given as[31,65,66]

$$\mathcal{L}_{VAE} = E\left[\log P\left(x|z\right)\right] - D_{KL}\left[Q\left(z|x\right) \| P\left(z\right)\right] \tag{3}$$

where E represents an expectation value, P and Q are probability distributions, D_{KL} represents the KL divergence, x is the binary vector representing the RN unit cells, and z represents the latent variables. $Q(z|x)$ and $P(x|z)$ are approximated by the recognition and reconstruction models, respectively. The incorporation of the conditional information in the loss function of the VAE modifies the loss function of CVAE as follows[65,66]

$$\mathcal{L}_{CVAE} = E\left[\log P\left(x|z, y\right)\right] - D_{KL}\left[Q\left(z|x, y\right) \| P\left(z|y\right)\right] \tag{4}$$

where y is a condition vector that plays an active role in both the encoding and decoding operations. The condition vector in the model contains the elastic properties of the RN unit cells.

To assess the elastic properties of the generated RN unit cells and as a regularisation term to the overall loss function[29] the pretrained "unit cell elastic properties model" that predicts the elastic properties of the RN unit cells was incorporated in the overall loss function ($\mathcal{L}_{all}$). $\mathcal{L}_{all}$ for the training of the deep generative model contains terms that account for the configuration of the latent space, the reconstruction of the input metamaterial design, and the retrieval of the desired elastic properties from the generated RN unit cells. For the retrieval of the desired mechanical properties from the reconstructed RN unit cells, MSE is considered as the loss function, $\mathcal{L}_{\mathrm{MSE}}$. Therefore, the total loss function for the deep generative model (Equation (5)) include those corresponding to the CVAE ($\mathcal{L}_{\mathrm{CVAE}}$) and the MSE ($\mathcal{L}_{\mathrm{MSE}}$) between the target and predicted elastic properties of the reconstructed RN unit cells

$$\mathcal{L}_{\mathrm{all}} = \mathcal{L}_{\mathrm{CVAE}} + \mathcal{L}_{\mathrm{MSE}} \tag{5}$$

To train a CVAE with an optimal fitting and a lower dimension of the latent space, the same hyperparamater tuning pipeline as for the unit cell elastic properties model was used. Some assumptions were made based on the best resulting parameters for the unit cell properties model. Identical hyperparameters as for the unit cell elastic properties model were used in the data processing steps. Additionally, the Adam optimizer was preselected, having outperformed the RMSprop optimizer in the training of the "unit cell properties model." In total, 6144 combinations of parameters were tested through the hyperparameter optimization method with a running time of ≈1341 min (≈23 h) (Table S7, Supporting Information). For the validation of the elastic properties arising from the generated RN unit cells and as a regularization term to the overall loss, the pretrained unit cell elastic properties model was used as a forward predictor of the elastic properties of the RN unit cells (E_{11}, E_{22}, ν_{12}, and ν_{21}).

For the evaluation of the trained CVAE (Figure S8, Supporting Information) with the help of the test dataset, the latent space was visualized to see if it is well-clustered. Moreover, the relevant performance metrics (i.e., Confusion matrix, Precision, Recall, and F_1 score) for the same purpose was used. To visualize the latent space (Figure S9a, Supporting Information) where the metamaterial design is encoded, the *t*-distributed stochastic neighbor embedding (*t*-SNE) approach was used to reduce its dimension to two. In addition to capturing the relevant information regarding the design of RN structures, the latent variables need to capture some information regarding the elastic properties of the designs. As a result, elastic properties are examined and distributed inside each geometric cluster. Because elastic properties are continuous and, thus, cannot be split into categories, they were manually classified according to certain specific criteria to investigate if the latent space can identify distinct Poisson's ratios to a satisfactory degree. The targets of the elastic properties are assigned to three classes: 0 for auxetic metamaterials, 1 for conventional metamaterials, and 2 for double-auxetic metamaterials. The binary multilabel class output is assessed in the case of unit cell representation reconstruction. This is accomplished by calculating the weighted average of the actual and predicted classes for each sample in the test dataset. The confusion matrix shows, in a sample-wise manner, the summary of the prediction results of the classification problem with each row corresponding to the actual class and each column corresponding to the predicted one. This matrix was then used to assess the classification accuracy of the model.

For the evaluation of the model training, the F_1 score (Figure S9b, Supporting Information) was chosen as the evaluation index of the introduced RN reconstruction, and the predicted elastic responses of the returned structures were evaluated using R^2. The F_1 score is mainly established for binary classification tasks with the values 1 and 0 corresponding to the best and worst performances, respectively. The F_1 score may be considered a weighted harmonic mean of the precision and recall, where the recall and precision are both equally essential (Equation (6)). Intuitively, precision is the proportion of the true positive cases among those labeled as positive by the model and recall is the proportion of the positive instances among the total number of positive examples including

$$F_1 = \frac{2 \times \mathrm{recall} \times \mathrm{precision}}{\mathrm{recall} + \mathrm{precision}}, \text{ where recall} = \frac{\mathrm{TP}}{\mathrm{TP} + \mathrm{FN}}, \text{ precision} = \frac{\mathrm{TP}}{\mathrm{TP} + \mathrm{FP}} \tag{6}$$

where TP is true positive, FN is false negative, and FP is false positive.

Deep Learning—Size-Agnostic Model: To predict the elastic properties of the combinatorial designs composed of RN unit cells with given dimensions, a forward predictor model referred to as the "size-agnostic model" was trained. This model aims to learn the mapping from the space of combinatorial designs composed of $D_1 \times D_2$ repetitions of RN unit cells (where D_1 and D_2 are the number of the repetitions of a RN unit cell along directions 1 and 2, respectively, and are assumed to be an even value in the range of (2–20)) to the space of their elastic properties (i.e., E_{11}, E_{22}, ν_{12}, and ν_{21}). A binary vector representing the RN unit cells combined with the vectors D_1 and D_2 were introduced to the model as inputs. The model returned the elastic properties of the combinatorial design as its output. Before training the model, the same hyperparameter tuning pipeline as described above for the unit cell elastic properties model was used to optimize the hyperparamaters of the model (Table S11, Supporting Information). MSE was assumed. (Equation (1)) as the loss function of the model and used R^2 (Equation (2)) and MSE (Equation (1)) for the evaluation of the trained model.

Experiments: Six RN unit cells (Figure 1b,c) and four combinatorial designs (Figure 3d) to be 3D printed and mechanically tested were selected. The SLS method for printing these lattices using a commercially available material (i.e., Oceanz Flexible TPU) was used. The 3D printed specimens were attached to the testing machine using a designed pin and gripper system which was 3D printed using a fused deposition modeling (FDM) 3D printer (Ultimaker 2+, Geldermalsen, the Netherlands) from polylactic acid (PLA) filaments (MakerPoint PLA, 750 gr, Natural). A mechanical testing machine (LLOYD instrument LR5K, load cell = 100 N) was used to perform quasistatic uniaxial tensile tests of the 3D printed specimens. The specimens were loaded at a rate of 0.05 mm min^{-1} until the maximum strain of 5% or a load of 95 N was reached along directions 1 and 2. The stress–strain curves were then obtained based on the applied displacements and the recorded reaction forces. Stress and strain values were calculated by dividing the force by the initial cross-section area and dividing the crosshead displacements by the initial length of the specimen, respectively. The overall stiffness of the specimens along directions 1 and 2 (i.e., E_{11} and E_{22}) were then calculated as the slope of the stress–strain curves. To calculate the Poisson's ratios (i.e., ν_{12} and ν_{21}) of the specimens, image analysis using a custom-made MATLAB code was performed. For this purpose, a digital camera was used to capture the lateral deformations of the specimens to measure the transverse strain at the different steps of the applied longitudinal displacement. Finally, the Poisson's ratio was calculated as $\nu = -\varepsilon_{\mathrm{trans}}/\varepsilon_{\mathrm{axial}}$, where $\varepsilon_{\mathrm{trans}}$ and $\varepsilon_{\mathrm{axial}}$ were calculated in the same way as in the computational models.

Full-field strain maps (first principal true strains) at a frequency of 1 Hz using a 3D DIC system (Q-400, two cameras each with 12 MPixel, LIMESS GmbH, Krefeld, Germany) and its associated software (Instra 4D v4.6, Danted Dynamics A/S, Skovunde, Denmark) were obtained. To track the internal displacements of the lattices, the specimens were painted with a white coating followed by a black-dot speckle pattern. The overall strain of the specimens and their Poisson's ratios were obtained using digital extensometers integrated within the DIC software. Due to their large sizes, the 10 × 10 unit cell specimens were not recorded with the DIC equipment and their overall strains were calculated using the crosshead displacement of the testing bench and their Poisson's ratio were calculated using the method described above.

The mechanical properties of these specimens were validated using FE simulations with the Abaqus solver. These simulations were carried out under the same conditions as mentioned in the previous sections. These simulations were performed under displacement control until the final strain of their respective experiment. An in-house made MATLAB code was used to obtain the coefficient of determination (Ordinary R^2) between the additional experiments and their simulations. The obtained values were $R^2 = 93.32\%$ for the elastic modulus and $R^2 = 80.2\%$ for the Poisson's ratio.

Supporting Information

Supporting Information is available from the Wiley Online Library or from the author.

Conflict of Interest

The authors declare no conflict of interest.

Data Availability Statement

The data that support the findings of this study are available from the corresponding author upon reasonable request.

Keywords

additive manufacturing, deep learning, numerical simulations, random-network mechanical metamaterials, size-agnostic, variational autoencoder

Received: April 14, 2023
Revised: October 6, 2023
Published online:

[1] H. M. A. Kolken, S. Janbaz, S. M. A. Leeflang, K. Lietaert, H. H. Weinans, A. A. Zadpoor, *Mater. Horiz.* **2018**, *5*, 28.
[2] G. L. Koons, M. Diba, A. G. Mikos, *Nat. Rev. Mater.* **2020**, *5*, 584.
[3] A. A. Zadpoor, *Biomater. Sci.* **2020**, *8*, 18.
[4] A. Rafsanjani, K. Bertoldi, A. R. Studart, *Sci. Rob.* **2019**, *4*, eaav7874.
[5] H. Lee, Y. Jang, J. K. Choe, S. Lee, H. Song, J. P. Lee, N. Lone, J. Kim, *Sci. Rob.* **2020**, *5*, eaay9024.
[6] S. Wu, Q. Ze, R. Zhang, N. Hu, Y. Cheng, F. Yang, R. Zhao, *ACS Appl. Mater. Interfaces* **2019**, *11*, 41649.
[7] J. U. Surjadi, L. Gao, H. Du, X. Li, X. Xiong, N. X. Fang, Y. Lu, *Adv. Eng. Mater.* **2019**, *21*, 1800864.
[8] W. Wu, W. Hu, G. Qian, H. Liao, X. Xu, F. Berto, *Mater. Des.* **2019**, *180*, 107950.
[9] M. J. Mirzaali, A. Ghorbani, K. Nakatani, M. Nouri-Goushki, N. Tümer, S. J. P. Callens, S. Janbaz, A. Accardo, J. Bico, M. Habibi, A. A. Zadpoor, *Adv. Mater.* **2021**, *33*, 2008082.
[10] A. A. Zadpoor, *Mater. Horiz.* **2016**, *3*, 371.
[11] E. Barchiesi, M. Spagnuolo, L. Placidi, *Math. Mech. Solids* **2019**, *24*, 212 .
[12] G. N. Greaves, A. L. Greer, R. S. Lakes, T. Rouxel, *Nat. Mater.* **2011**, *10*, 823.
[13] K. Bertoldi, V. Vitelli, J. Christensen, M. Van Hecke, *Nat. Rev. Mater.* **2017**, *2*, 17066.
[14] X. Zheng, H. Lee, T. H. Weisgraber, M. Shusteff, J. Deotte, E. B. Duoss, J. D. Kuntz, M. M. Biener, Q. Ge, J. A. Jackson, S. O. Kucheyev, N. X. Fang, C. M. Spadaccini, *Science* **2014**, *344*, 1373.
[15] G. Ma, P. Sheng, *Sci. Adv.* **2016**, *2*, e1501595.
[16] S. A. Cummer, J. Christensen, A. Alù, *Nat. Rev. Mater.* **2016**, *1*, 16001.
[17] M. Kadic, T. Bückmann, R. Schittny, M. Wegener, *Rep. Prog. Phys.* **2013**, *76*, 126501.
[18] S. Amin Yavari, S. M. Ahmadi, R. Wauthle, B. Pouran, J. Schrooten, H. Weinans, A. A. Zadpoor, *J. Mech. Behav. Biomed. Mater.* **2015**, *43*, 91.
[19] H. Pahlavani, M. Amani, M. C. Saldívar, J. Zhou, M. J. Mirzaali, A. A. Zadpoor, *Commun. Mater.* **2022**, *3*, 46.
[20] S. Maraghechi, J. P. M. Hoefnagels, R. H. J. Peerlings, O. Rokoš, M. G. D. Geers, *Mater. Des.* **2020**, *193*, 108684.
[21] M. J. Mirzaali, H. Pahlavani, A. A. Zadpoor, *Appl. Phys. Lett.* **2019**, *115*, 021901.
[22] M. Hanifpour, C. F. Petersen, M. J. Alava, S. Zapperi, *Eur. Phys. J. B* **2018**, *91*, 271.
[23] D. Rayneau-Kirkhope, S. Bonfanti, S. Zapperi, *Appl. Phys. Lett.* **2019**, *114*, 111902.
[24] V. F. Hagh, M. F. Thorpe, *Phys. Rev. B* **2018**, *98*, 100101.
[25] D. R. Reid, N. Pashine, J. M. Wozniak, H. M. Jaeger, A. J. Liu, S. R. Nagel, J. J. De Pablo, *Proc. Natl. Acad. Sci. USA* **2018**, *115*, E1384.
[26] W. Ma, F. Cheng, Y. Xu, Q. Wen, Y. Liu, *Adv. Mater.* **2019**, *31*, 1901111.
[27] L. Wang, Y.-C. Chan, F. Ahmed, Z. Liu, P. Zhu, W. Chen, *Comput. Methods Appl. Mech. Eng.* **2020**, *372*, 113377.
[28] H. T. Kollmann, D. W. Abueidda, S. Koric, E. Guleryuz, N. A. Sobh, *Mater. Des.* **2020**, *196*, 109098.
[29] S. Kumar, S. Tan, L. Zheng, D. M. Kochmann, *npj Comput. Mater.* **2020**, *6*, 73.
[30] I. Goodfellow, J. Pouget-Abadie, M. Mirza, B. Xu, D. Warde-Farley, S. Ozair, A. Courville, Y. Bengio, *Commun. ACM* **2020**, *63*, 139.
[31] D. P. Kingma, M. Welling, ArXiv: 1312.6114, **2013**.
[32] Y. Pathak, K. S. Juneja, G. Varma, M. Ehara, U. D. Priyakumar, *Phys. Chem. Chem. Phys.* **2020**, *22*, 26935.
[33] Y. Dan, Y. Zhao, X. Li, S. Li, M. Hu, J. Hu, *npj Comput. Mater.* **2020**, *6*, 84.
[34] T. Xue, T. J. Wallin, Y. Menguc, S. Adriaenssens, M. Chiaramonte, *Extreme Mech. Lett.* **2020**, *41*, 100992.
[35] B. Sanchez-Lengeling, A. Aspuru-Guzik, *Science* **2018**, *361*, 360.
[36] M. J. Buehler, *Modell. Simul. Mater. Sci. Eng.* **2023**, *31*, 054001.
[37] A. J. Lew, M. J. Buehler, *Mater. Today* **2023**, *64*, 10.
[38] Z. Yang, Y.-C. Hsu, M. J. Buehler, *J. Mech. Phys. Solids* **2023**, *170*, 105098.
[39] D. P. Kingma, J. A. Ba, ArXiv: 1412.6980, **2014**.
[40] S. Oh, Y. Jung, S. Kim, I. Lee, N. Kang, *J. Mech. Des.* **2019**, *141*, 111405.
[41] S. Oh, Y. Jung, S. Kim, I. Lee, N. Kang, *Proc. Des. Soc.: Des. Conf.* **2020**, *1*, 460.
[42] K. Guo, M. J. Buehler, *Extreme Mech. Lett.* **2020**, *41*, 101029.
[43] Z. Yang, M. J. Buehler, *npj Comput. Mater.* **2022**, *8*, 198.
[44] K. Guo, M. J. Buehler, *Digital Discovery* **2022**, *1*, 277.
[45] J. Henriksson, C. Berger, M. Borg, L. Tornberg, S. R. Sathyamoorthy, C. Englund, *Inf. Software Technol.* **2021**, *130*, 106409.
[46] S. Liang, Y. Li, R. Srikant, ArXiv: 1706.02690, **2017**.
[47] M. W. Browne, *J. Math. Psychol.* **2000**, *44*, 108.
[48] P. Refaeilzadeh, L. Tang, H. Liu, in *Encyclopedia of Database Systems*, (Eds: L. Liu, M. Tamer ÖZsu), Springer, New York, **2009**, pp. 532–538.
[49] H. Reed, J. Cipolla, P. Murray, *J. Acoust. Soc. Am.* **2015**, *138*, 1910.
[50] A. P. Garland, B. C. White, S. C. Jensen, B. L. Boyce, *Mater. Des.* **2021**, *203*, 109632.
[51] S. Sankararaman, K. McLemore, S. Mahadevan, in *Topics in Model Validation and Uncertainty Quantification, Vol. 4, Conference Proceedings of the Society for Experimental Mechanics Series* (Eds: T. Simmermacher, S. Cogan, L. G. Horta, R. Barthorpe), Springer, New York, pp. 67–74.
[52] R. Arróyave, D. Khatamsaz, B. Vela, R. Couperthwaite, A. Molkeri, P. Singh, D. D. Johnson, X. Qian, A. Srivastava, D. Allaire, *MRS Commun.* **2022**, *12*, 1037.
[53] P. I. Frazier, J. Wang, in *Information Science for Materials Discovery and Design* (Eds: T. Lookman, F. J. Alexander, K. Rajan), Springer International Publishing, Cham, Switzerland, **2016**, pp. 45–75.
[54] M. A. Bessa, P. Glowacki, M. Houlder, *Adv. Mater.* **2019**, *31*, 1904845.
[55] A. J. Lew, M. J. Buehler, *Forces. Mech.* **2021**, *5*, 100054.
[56] D. Rajagopal, A. Koeppe, M. Esmaeilpour, M. Selzer, W. Wenzel, H. Stein, B. Nestler, *Adv. Energy Mater.* **2023**, *13*, 2301985.
[57] D. Yan, A. D. Smith, C.-C. Chen, *Nat. Comput. Sci.* **2023**, *3*, 572.
[58] S. C.-Y. Shen, M. J. Buehler, *Commun. Eng.* **2022**, *1*, 37.
[59] M. J. Mirzaali, V. Moosabeiki, S. M. Rajaai, J. Zhou, A. A. Zadpoor, *Materials* **2022**, *15*, 5457.
[60] E. Yarali, A. A. Zadpoor, U. Staufer, A. Accardo, M. J. Mirzaali, *ACS Appl. Bio. Mater.* **2023**, *6*, 2562.

[61] A. A. Zadpoor, M. J. Mirzaali, L. Valdevit, J. B. Hopkins, *APL Mater.* **2023**, *11*, 020401.

[62] W. Shi, J. Cao, Q. Zhang, Y. Li, L. Xu, *IEEE Internet Things J.* **2016**, *3*, 637.

[63] J. Chen, X. Ran, *Proc. IEEE Inst. Electr. Electron. Eng.* **2019**, *107*, 1655.

[64] T. H. Cormen, C. E. Leiserson, R. L. Rivest, C. Stein, *Introduction to Algorithms*, MIT Press, Cambridge, MA, USA **2022**.

[65] J. Lim, S. Ryu, J. W. Kim, W. Y. Kim, *J. Cheminf.* **2018**, *10*, 31.

[66] K. Sohn, H. Lee, X. Yan, in *NIPS'15: Proc. 28th Int. Conf. on Neural Information Processing Systems, Vol. 2 December 2015*, ACM, New York **2015**, pp. 3483–3491.